ARL-TR-10309 • MAR 2026

The Quasi-Static and Dynamic Thermomechanical Behavior of Medium-Mn Steels with Different Stacking Fault Energies

by Christopher S. Meredith, Daniel J. Magagnosc, Daniel M. Field, Timothy R. Walter, Jeffrey T. Lloyd, and Krista R. Limmer

NOTICES

Disclaimers

ARL-TR-10309 ● MAR 2026

The Quasi-Static and Dynamic Thermomechanical Behavior of Medium-Mn Steels with Different Stacking Fault Energies

Christopher S. Meredith, Daniel J. Magagnosc, Daniel M. Field, Timothy R. Walter, Jeffrey T. Lloyd, and Krista R. Limmer

DEVCOM Army Research Laboratory

REPORT DOCUMENTATION PAGE

1. REPORT DATE March 2026	**2. REPORT TYPE** Technical Report	**3. DATES COVERED** **START DATE** October 2018	**END DATE** September 2021

4. TITLE AND SUBTITLE
The Quasi-Static and Dynamic Thermomechanical Behavior of Medium-Mn Steels with Different Stacking Fault Energies

5a. CONTRACT NUMBER	**5b. GRANT NUMBER**	**5c. PROGRAM ELEMENT NUMBER**
5d. PROJECT NUMBER	**5e. TASK NUMBER**	**5f. WORK UNIT NUMBER**

6. AUTHOR(S)
Christopher S. Meredith, Daniel J. Magagnosc, Daniel M. Field, Timothy R. Walter, Jeffrey T. Lloyd, and Krista R. Limmer

7. PERFORMING ORGANIZATION NAME(S) AND ADDRESS(ES) DEVCOM Army Research Laboratory ATTN: FCDD-RLA-TB Aberdeen Proving Ground, MD 21005	**8. PERFORMING ORGANIZATION REPORT NUMBER** ARL-TR-10309

9. SPONSORING/MONITORING AGENCY NAME(S) AND ADDRESS(ES)	**10. SPONSOR/MONITOR'S ACRONYM(S)**	**11. SPONSOR/MONITOR'S REPORT NUMBER(S)**

12. DISTRIBUTION/AVAILABILITY STATEMENT
DISTRIBUTION STATEMENT A. Approved for public release: distribution unlimited.

13. SUPPLEMENTARY NOTES
ORCIDs: Christopher S. Meredith, 0000-0003-1368-8003; Daniel J. Magagnosc, 0000-0002-1418-9292; Daniel M. Field, 0000-0002-8890-4391; Timothy R. Walter, 0000-0002-1786-3668; Krista R. Limmer, 0000-0003-4775-5876

14. ABSTRACT
We present the mechanical behavior of three different advanced high-strength steels that share an iron–manganese–aluminum–chromium–carbon base composition with stacking-fault energies (SFEs) tailored by adjusting alloy composition to obtain transformation-induced plasticity (TRIP), twinning-induced plasticity (TWIP), or perfect glide of dislocations (referred to as Slip). The Slip alloy (SFE = 49.3 mJ/m^2) was a duplex alloy consisting mostly of γ-austenite with some δ-ferrite; the TWIP alloy (SFE = 26.9 mJ/m^2) was fully austenitic; and the TRIP steel (SFE = 3.9 mJ/m^2) was a triplex alloy consisting of austenite, α-martensite, and ε-martensite. The mechanical behavior of the three alloys was measured as functions of strain rate, temperature, and load path (tension or compression) to determine how the plastic behavior changes. Results show the Slip alloy has the highest yield strength but lowest work-hardening rate; the TRIP has the lowest yield strength and highest work-hardening rate; and the TWIP is between the other two, at room temperature at both quasi-static and dynamic (~10^3 s^{-1}) strain rates and in tension and compression. At a 200 °C testing temperature, the Slip and TWIP alloys' strengths drop as expected, but the work-hardening rates change little, while the TRIP alloy yield strength increases and hardening rate drastically decreases. Thus, increasing the temperature tends to homogenize the behavior of the three alloys to where there are only small differences in strength and hardening. The strain-rate sensitivity of the Slip and TWIP is a positive number for the strength while changing the hardening little, with the TRIP alloy being the opposite. These trends in behavior are discussed in terms of how the SFE changes under various experimental conditions, with the rise of the SFE with temperature being dominant in shifting the deformation mechanisms.

15. SUBJECT TERMS
twinning-induced plasticity, TWIP steel, transformation-induced plasticity, TRIP steel, medium-manganese steel, medium-Mn steel, stacking-fault energy, martensitic transformation, mechanical twinning, Sciences of Extreme Materials, Terminal Effects

16. SECURITY CLASSIFICATION OF:			**17. LIMITATION OF ABSTRACT**	**18. NUMBER OF PAGES**
a. REPORT	**b. ABSTRACT**	**C. THIS PAGE**		
UNCLASSIFIED	UNCLASSIFIED	UNCLASSIFIED	UU	30

19a. NAME OF RESPONSIBLE PERSON Christopher S. Meredith	**19b. PHONE NUMBER** *(Include area code)* (520) 691-6413

STANDARD FORM 298 (REV. 5/2020)
Prescribed by ANSI Std. Z39.18

Contents

List of Figures

List of Tables

Acknowledgments

Thanks to Levi Johnson (University of Maryland, Baltimore County) for performing many of the dynamic experiments and Jason Garvey (ARL) for helping with the experiments too.

1. Introduction

The mechanisms at multiple length scales that control deformation and failure under dynamic loading of advanced high-strength steels (AHSS) are poorly understood, and understanding them is critically important to their wider use. Several new formulations of AHSS have been developed since 2000 for the automotive industry that have target tensile strengths above 1200 MPa and total ductility greater than or equal to 25%. Recent AHSS alloy investigations often focused on mixed microstructures of austenite, α-martensite/δ-ferrite, and ε-martensite obtained by alloying with elevated concentrations of manganese (Mn), aluminum (Al), and silicon (Si).[1–7] These novel steel alloys have been shown to delay necking for increased total elongation and elevated work-hardening rates, which are of significant interest to the automotive industry for both crashworthiness and formability of complex parts. However, these investigations were all of sheet gauge (~1 mm) and are produced by hot rolling followed by cold rolling and annealing, which is not necessarily suitable to a use case where thicker plates are required. These alloys have been shown to deform by a combination of mechanisms: deformation-induced transformation, mechanical twinning, and perfect dislocation glide.[1,4,6,8–10] It is well understood that the stacking-fault energy (SFE) dictates the deformation mechanisms of the austenite phase.[4,6,9,10] Alloys are typically classified into three groups based on their calculated SFE. Alloys with a SFE less than or equal to 15 mJ/m^2 typically exhibit deformation-induced transformation, also known as transformation-induced plasticity (TRIP), in which the austenite transforms into ε-martensite or α-martensite under an imposed stress.[1,3,9–12] When the SFE is between 20–45 mJ/m^2, mechanical twinning, known as twinning-induced plasticity (TWIP), generally occurs.[2,9,10,13] Lastly, if the SFE is greater than 45 mJ/m^2, dislocations are not able to separate to form partials, and they move by glide or slip. These delineations are somewhat arbitrary and alloys near a boundary can and do have a combination of mechanisms active during deformation. By fine-tuning the alloying component amounts, such as Mn, Al, and carbon (C), steel alloys can be created that will exhibit one of the three deformation mechanisms.

TWIP and TRIP steels offer the potential of obtaining relatively high ultimate strengths without sacrificing ductility. This balance of properties is achieved by high work-hardening rates due to the dynamic Hall–Petch effect, whereby austenitic grains are subdivided by either twins or phase boundaries (ε/α-martensite) during deformation.[8,12,13] The increased total ductility has been historically attributed to delaying the onset of necking.[14,15] However, a weakness of these alloys is that since they are fully or primarily austenitic, they have a relatively low yield strength compared with industrial AHSS currently in use because twinning and transformation have a lower critical resolved shear stress than dislocation glide.[2,12] To combat this issue, alloys typically have been processed to refine the grain structure to improve the yield strength[4–7]; however, in the hot-rolled condition, these alloys typically exhibit yield strengths as low as 200 MPa.[3–5,7,13,16–19]

Little work has been reported evaluating the high strain rate or temperature effects on the mechanical response of these alloys, especially with respect to impact testing, which has shown no improvement so far over conventional steel.[20] Additionally, while previous studies on medium-Mn steels have investigated the effect of SFE on the deformation mechanisms and mechanical behavior, no known study has comprehensively examined the full range of these effects. For example, Pozuelo et al.[8] evaluated a large range of SFE values by varying the temperature, but this was done on only one composition. Additionally, Curtze and Kuokkala[13] performed a more intensive study using four different compositions while varying temperature and strain rate, but they were all TWIP steels. This report is a more comprehensive study on the effects of temperature and strain rate on the mechanical behavior of iron–manganese–aluminum–chromium–carbon (Fe–Mn–Al–Cr–C) base composition alloys that span the slip, TWIP, and TRIP mechanism regimes. In this study, we created and processed three formulations of steel plate with varying Al and C concentrations to vary the SFE, such that each of the regimes is represented. The mechanical behavior of each formulation was measured in compression and tension at quasi-static and dynamic strain rates and at testing temperatures between room temperature and 200 °C. We describe the changes in the mechanical behavior under the different conditions in terms of the SFE and the underlying slip, TWIP, or TRIP deformation mechanisms.

2. Experimental Procedures

Three steel alloys were vacuum-induction melted and cast into 25-kg ingots with dimensions of 145 × 360 × 50 mm^3. Chemical analyses were obtained by inductively coupled plasma spectrometry after sample dissolution in hydrochloric and nitric acids. Carbon content was determined using gas combustion analysis. Alloy composition and calculated room temperature SFE are listed in Table 1. For brevity, the alloys are designated by their anticipated room temperature deformation mode (Slip, TWIP, or TRIP) according to the SFE value calculated using Olson and Cohen's formulation[21]:

$$\mathrm{SFE}\ (\mathrm{mJ/m^2}) = n\rho(\Delta G^{\gamma\rightarrow\varepsilon}) + 2\sigma^{\gamma/\varepsilon}\ .$$

The stacking-fault embryo size was $n = 2$; the interfacial energy between the γ-austenite and ε-martensite was $\sigma^{\gamma/\varepsilon} = 10$ mJ/m^2, according to the results of Pisarik and Van Aken[22]; the driving force for the γ-austenite to ε-martensite transformation, $\Delta G^{\gamma\rightarrow\varepsilon}$, was obtained using an updated regular solution model[22]; and the planar atomic density of the $(111)_\gamma$, ρ, was calculated using alloy chemistry and Vegard's law.

Table 1. Composition and calculated SFE of each alloy.

Alloy	Composition (wt%)					SFE
	C	Al	Mn	Cr	Si	(mJ/m^2)
Slip	0.61	5.0	13.0	3.5	1.01	49.3
TWIP	0.61	2.0	13.0	3.5	0.99	26.9
TRIP	0.16	0.5	12.8	3.4	0.98	3.9

The steel castings were normalized at 1250 °C for 2 h and air cooled to room temperature, then hot rolled by heating to 1100 °C, rolling, and reheating with an IR pyrometer when the surface temperature dropped below 800 °C. This was repeated to obtain a plate thickness of 12.5 ± 5 mm. The total hot reduction was 73% ± 8%, and an exit temperature of 827 ± 50 °C was measured after the final roll pass to the desired hot band thickness. Finally, the as-rolled plates were recovery annealed by heating them to 650 °C for 2 h followed by air cooling.

Specimens for microscopy analysis were prepared from the annealed plates with the examination surface perpendicular to the rolling plane normal and the rolling direction. Specimens were mechanically polished for electron backscatter diffraction (EBSD) with a final stage of 0.020-µm colloidal silica solution using a vibratory polisher. Orientation image mapping was performed via pattern analysis on an FEI NanoSEM operated at an accelerating voltage of 20.0 kV and emission current of 2.7 nA.

All experiments probing the quasi-static and dynamic mechanical behaviors were performed with the loading direction parallel to the rolling direction of the plate. The experiment was performed at least three times for each testing parameter to ensure consistent results. All samples were machined from the source plates using electro-discharge machining.

Quasi-static uniaxial compression and tension experiments were performed at a strain rate of approximately 10^{-3} s^{-1} at room temperature and 200 °C using a hydraulic load frame. The compression samples were cylindrical with a diameter and length equal to nominally 9.5 mm. The tension samples conformed to the American Society for Testing and Materials E8 subsize geometry. The elevated temperature experiments were performed with a furnace that surrounds the sample and loading platens. Strain was measured using digital image correlation (DIC) by taking images of the black-and-white–speckled sample surface as it deformed, and the force was measured for each image taken.

Dynamic compression experiments were performed with a standard Kolsky (or split-Hopkinson pressure) bar. The bars were maraging steel C350 with a diameter of 12.7 mm and lengths of 1825 and 457 mm for the incident and transmitted bars and striker, respectively. Compression samples were cubes with a side length of 4.57 mm and the rolling, transverse, and normal directions were tracked during machining to ensure the samples were always loaded in the rolling direction. The incident wave was pulse shaped using a copper disc with nominal dimensions of 7.9 × 1.1 mm. The compressive stress, strain, and strain rate of the samples were measured using the typical equations for this technique,[23,24] and equilibrium was confirmed for every experiment to ensure valid results. The nominal strain rate in compression was 2500 s^{-1}. Dynamic tension experiments were performed with a direct tension Kolsky bar setup, where an impedance/area matched tubular striker surrounding the incident bar is accelerated toward the free-end of the incident bar. The striker impacts a cap attached to the end of the incident bar and generates an elastic tension wave that travels toward the sample. The bars were Al 7075-T6 with a diameter of 15.9 mm and lengths of 3048, 1825, and 610 mm for the incident, transmitted, and tubular striker bars, respectively. The samples were flat dogbones with a hole in each gripping section. The sample fit into a slot cut into the bars and a shoulder bolt acted as a cross pin, applying a clamping pressure to the samples. A schematic of the gripping between the sample and bars is shown in Figure 1a, while Figure 1b provides the sample dimensions. The nominal strain rate in tension was between approximately 1500 and 3200 s^{-1} across all the experiments.

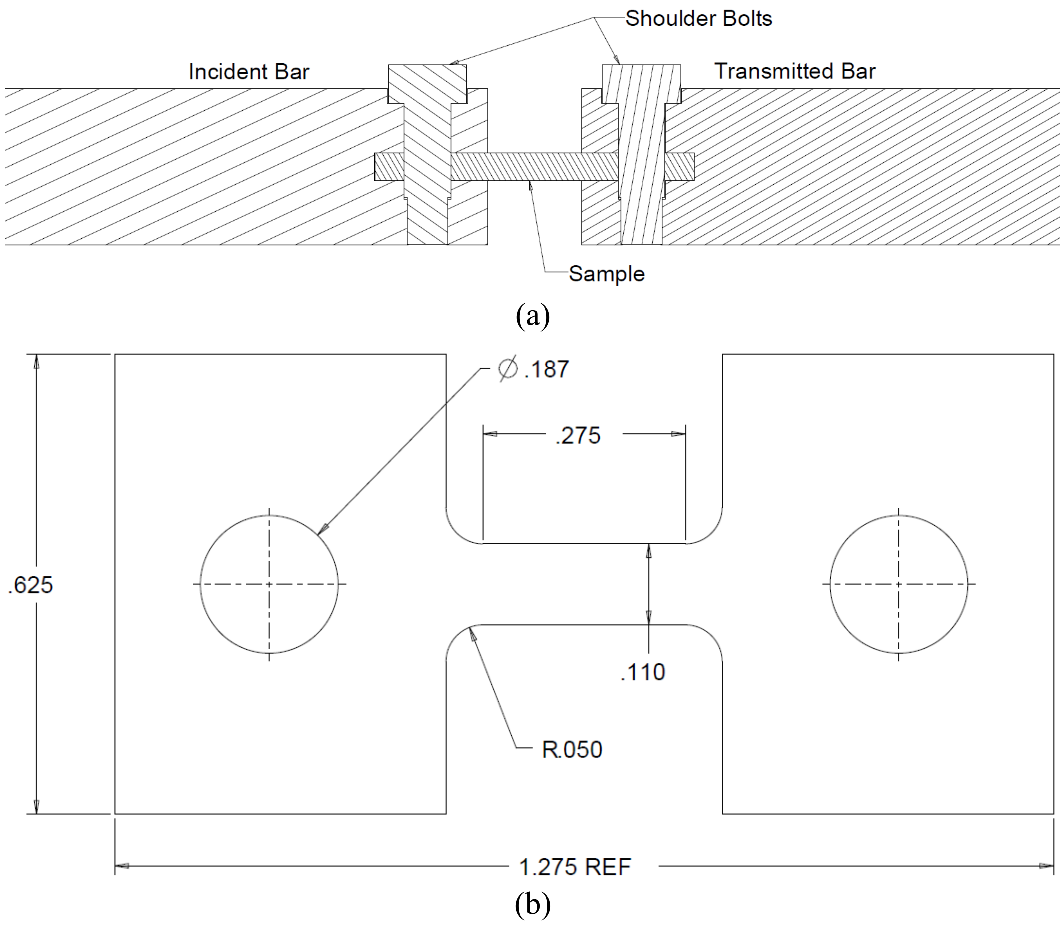

Figure 1. (a) Cross-sectional view of sample gripping in the tension Kolsky bar. (b) Engineering drawing of tension Kolsky bar samples (all units in inches).

Elevated temperature experiments were performed in both dynamic compression and tension using the same setups used for room temperature. The samples were heated via IR spot heaters that focus the energy to a spot size of approximately 6.4 mm. Three heaters were arranged every 120° around the sample, with all three pointed at it. This ensured all surfaces of the sample were bathed in IR radiation resulting in uniform sample temperature. The temperature was measured using a K-type thermocouple spot-welded to the sample that provided feedback to a proportional–integral–derivative controller that controlled the spot heaters. The thermocouple junction on the surface was covered with high-temperature cement to ensure the actual sample surface temperature was being measured and not the temperature from the IR radiation bathing the thermocouple. The time between starting the heaters and shooting was approximately 2–3 min, with the desired temperature held for approximately 30 s prior to shooting to ensure the sample's volume was at a uniform temperature. No corrections to the compression or tension Kolsky bar signals due to the heating of the bars were made because the change in Young's modulus or wave speed is negligible at 200 °C or less.

The gage section strain of dynamic tension samples was measured using DIC. For the room temperature experiments, a black-and-white–speckled pattern was applied using spray paint. The white base coat was a rubberized spray paint that did not crack or peel off, even at true strains of greater than 50%. For the elevated temperature experiments, the spray paint was too brittle; thus, lines from a silver-colored marker were drawn on the sample surface, perpendicular to the loading direction. The gray-scale difference between the lines and base metal surface was used to threshold the images and a MATLAB point-tracking program was used to calculate the average strain for each image. This method was validated against DIC at room temperature. The camera was a Shimadzu HPV-X2 high-speed camera at 400,000 fps with a 200-ns exposure time, which takes 128 images at a pixel resolution of 400 × 250. The sample was illuminated with a pair of Photogenic PL2500DRC strobes. Each camera image was time-correlated to the strain gages on the Kolsky bars via a common trigger, and the strain gage sampling rate was an integer multiple of the camera fps to enable easy time synchronization between the data.

3. Results

The SFE energy of the alloys chosen for this work was primarily controlled by modifying the weight percent of Al and C, where decreasing the Al content reduces the SFE and C additions raise it.[25] The as-processed alloys varied in the phases present as measured by EBSD (Table 2). The Slip alloy was a duplex steel consisting of 75.8-wt% γ-austenite and 24.2-wt% δ-ferrite; the TWIP alloy was fully austenitic; and the TRIP was a triplex alloy consisting of 34.4-wt% austenite, 16.8-wt% α-martensite, and 48.8-wt% ε-martensite. Figures 2 and 3 show the phase and orientation maps, respectively, of each alloy from EBSD scans. The fine-grained δ-ferrite in the slip is primarily segregated to the coarse-grained austenite grain boundaries, and forms bands along the grain boundaries. The area weighted grain size of the austenite grains is 105 µm, whereas the ferrite bands are 8.8 µm. Both phases are relatively equiaxed and a few austenite grains show evidence of annealing twins. The crystallographic texture of each phase was relatively weak, approximately 2.5 MRD for both the austenite and ferrite. The fully austenitic TWIP has an average grain size of 55 µm, with annealing twins present in many grains. Texture is also relatively weak. The as-processed TRIP alloy, with the lowest SFE, has a significantly more complicated microstructure, where no phase has a majority. The large fraction of ε-martensite is expected because it is the intermediate phase during the $\gamma \rightarrow \alpha$ phase transformation; however, the phase transformation generally did not go to completion since the α-martensite is only 16.8 vol%. All three phases form a banded microstructure.

Table 2. Phase alloy wt% according to EBSD.

Alloy	γ-austenite (wt%)	ε-martensite (wt%)	α-martensite or δ-ferrite (wt%)
Slip	75.8	. . .	24.2
TWIP	100	. . .	. . .
TRIP	34.4	48.8	16.8

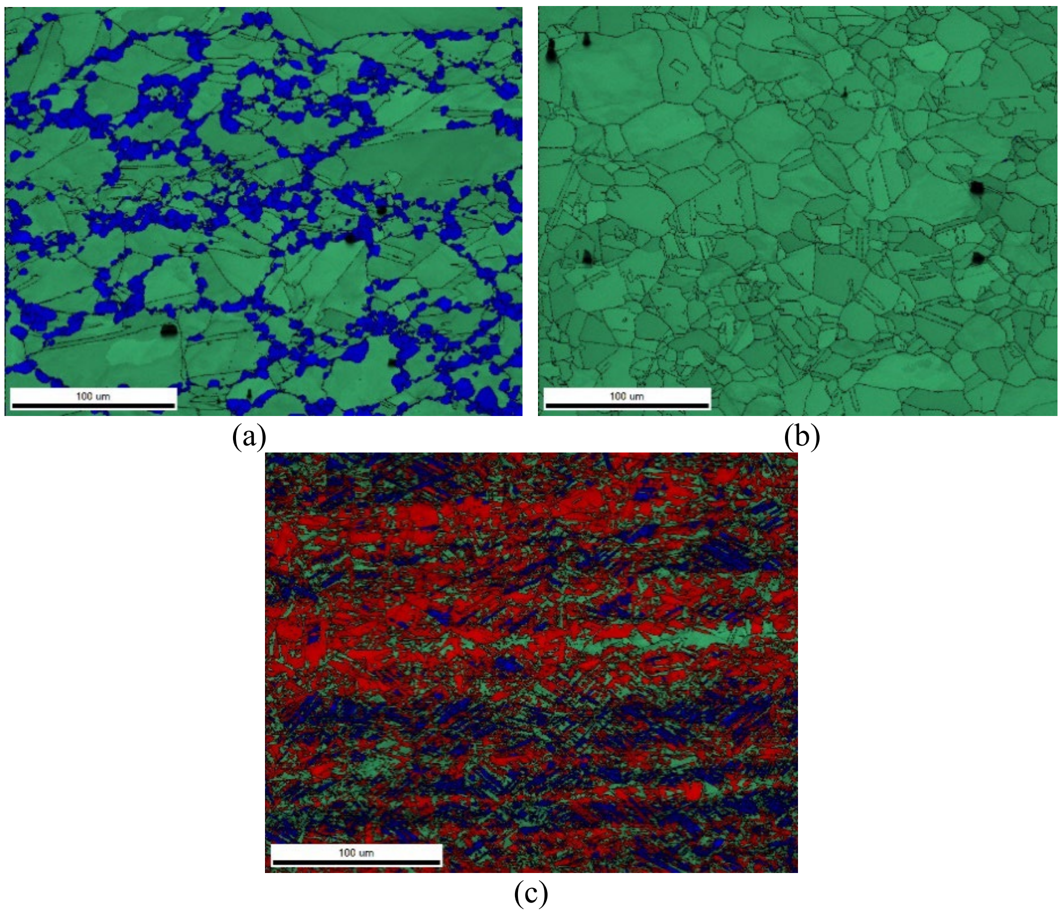

Figure 2. EBSD-generated phase maps of the (a) Slip, (b) TWIP, and (c) TRIP alloys. γ-austenite is shown in green, α-martensite/δ-ferrite is shown in blue, and ε-martensite is shown in red.

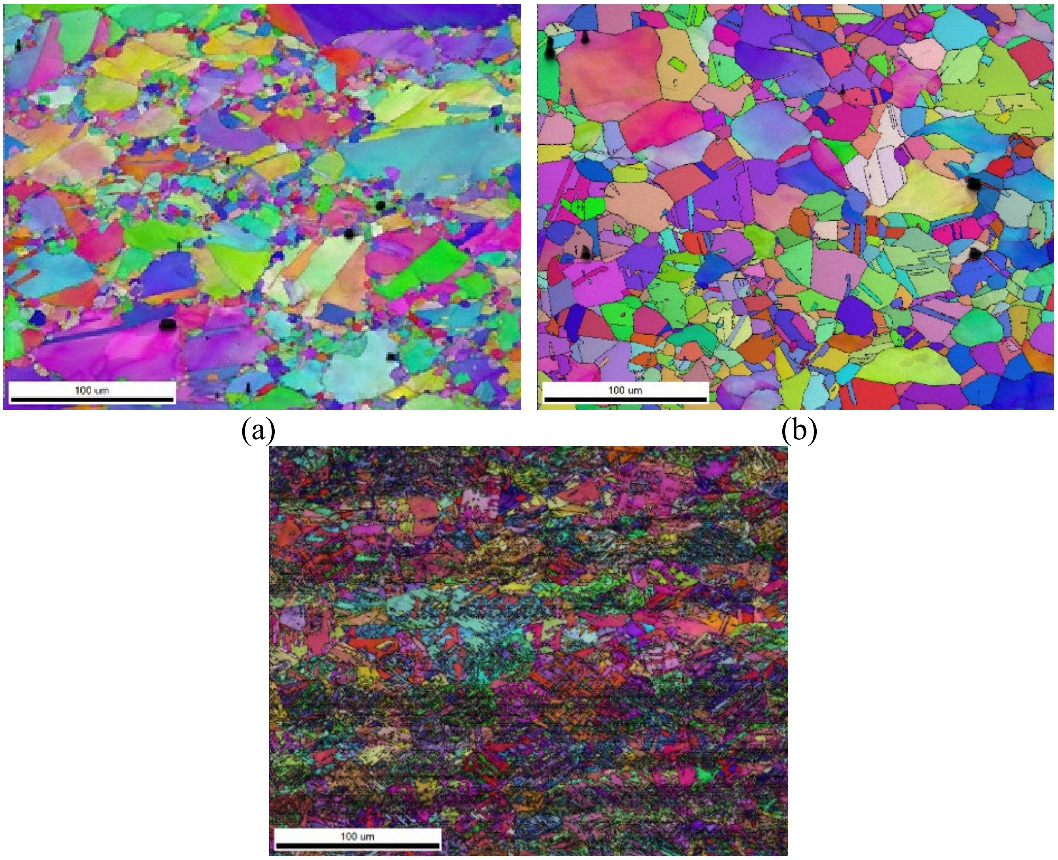

(a) (b)

(c)

Figure 3. EBSD-generated orientation image maps of microstructure maps of the (a) Slip, (b) TWIP, and (c) TRIP alloys.

Figures 4–7 summarize the true stress–strain mechanical behaviors of the Slip, TWIP, and TRIP alloys as functions of strain rate, load path (i.e., tension and compression), and temperature. A single representative true stress–strain curve is shown for each condition for clarity. In all the figures, solid and dashed curves correspond to dynamic and quasi-static strain rates, respectively. Additionally, sudden drops in the curves at large strains represent sample failure. Thus, in compression, no samples failed at quasi-static and dynamic strain rates during tension. Testing samples typically failed during dynamic loading with the singular exception of the TRIP steel. The three alloys' key mechanical properties as functions of strain rate, temperature, and load path are summarized in Table 3. Those values with standard deviations are calculated from three or four separate experiments. Yield strengths and true strain-to-failure in dynamic tension were only approximated, and ultimate strengths were not calculated, because the dynamic tension responses were interpolated. Finally, dynamic compression yield strengths of the TWIP alloy were approximated due to oscillations in measured responses at the yield point (Figure 6a), which is generally attributed to wave dispersion and other 3D wave effects. The oscillations in true stress varied by less than 50 MPa, and the sample-to-sample variation was much smaller than that, so no standard deviation was determined.

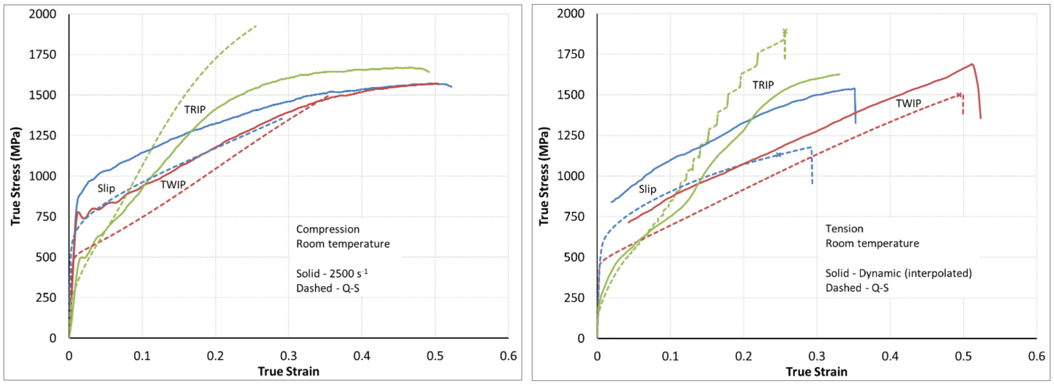

(a) (b)

Figure 4. Room temperature quasi-static and dynamic true stress–strain responses of Slip, TWIP, and TRIP steels in (a) compression and (b) tension. The dynamic tension responses are interpolated (see Appendix).

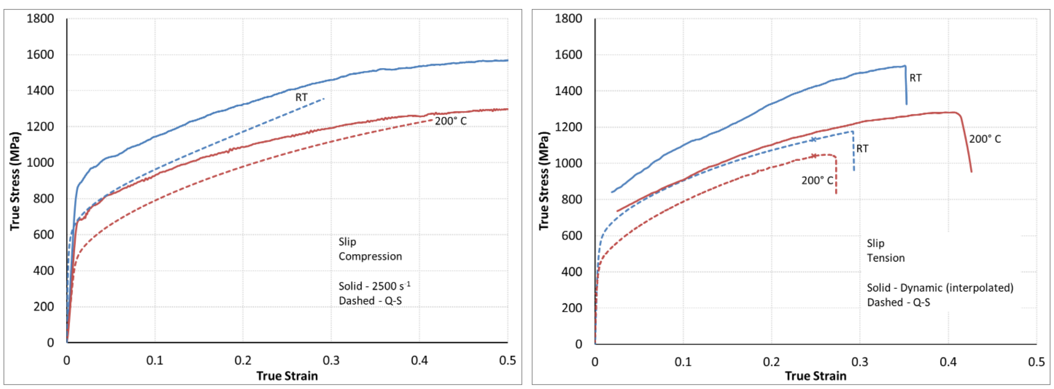

(a) (b)

Figure 5. Quasi-static and dynamic true stress–strain responses of Slip steel at different temperatures in (a) compression and (b) tension. The dynamic tension responses are interpolated (see Appendix).

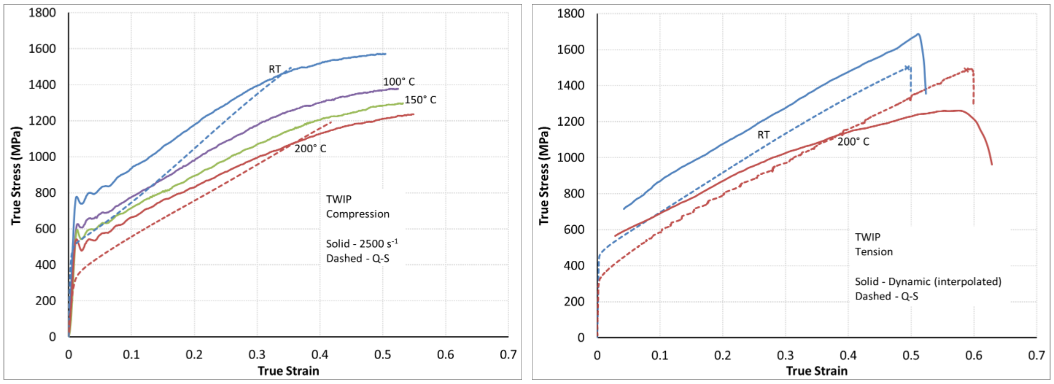

(a) (b)

Figure 6. Quasi-static and dynamic true stress–strain responses of TWIP steel at different temperatures in (a) compression and (b) tension. The dynamic tension responses are interpolated (see Appendix).

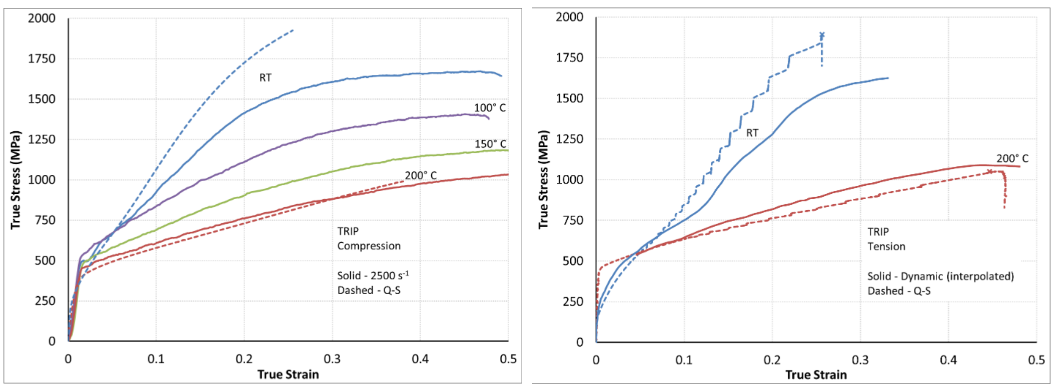

(a) (b)

Figure 7. Quasi-static and dynamic true stress–strain responses of TRIP steel at different temperatures in (a) compression and (b) tension. The dynamic tension responses are interpolated (see Appendix).

Table 3. Measured mechanical properties of the Slip, TWIP, and TRIP alloys as functions of strain rate, temperature, and load path.

Alloy	Strain rate	Temperature (°C)	Yield strength (MPa)	Tension ultimate strength (MPa)	Strain-to-failure (%)	Compression yield strength (MPa)
Slip	Quasi-static	22	552 ± 7	1185 ± 24	29.8 ± 2	587 ± 16
		200	461 ± 13	1037 ± 9	24.6 ± 2	472 ± 11
	Dynamic	22	~800	. . .	~35	875 ± 30
		200	~700	. . .	~41	683 ± 1
TWIP	Quasi-static	22	465 ± 0	1500 ± 7	49.7 ± 0	451 ± 8
		200	344 ± 15	1594 ± 74	71.4 ± 9	332 ± 14
	Dynamic	22	~610	. . .	~52	~750
		200	~510	. . .	~58	~505
TRIP	Quasi-static	22	175 ± 5	1837 ± 63	25.0 ± 1	286 ± 6
		200	454 ± 4	1080 ± 29	50.8 ± 4	357 ± 11
	Dynamic	22	~250	. . .	Did not fail	470 ± 14
		200	~425	. . .		463 ± 1

The dynamic tension data requires further explanation. Each dynamic true stress–strain curve is a single interpolated curve at each condition. Each curve was manually interpolated from at least three separate experiments taken to different levels of true strain. This interpolation was required because of the well-known pseudo-yield point stress response that often occurs with tension Kolsky bar data[26] that manifests as an abnormal stress peak at and following yielding of the specimen. The cause is the inertia difference between the incident and transmitted sides of the relatively "long" sample that is inherently required for establishing a uniaxial tensile stress state (plus gripping both ends of the sample). Factors such as a high-strength and high-ductility material exacerbate the pseudo-stress peak and extend it to a greater strain because they require the incident wave to be of larger magnitude; i.e., higher velocity of the incident end pulling on the sample, which magnifies the inertia difference. Both factors are present with these Slip, TWIP, and TRIP alloys. Thus, the complete true stress–strain response under dynamic tension was established with three separate experiments: a relatively low total strain test where the abnormal yield peak was minimal (but still present), a test where the sample was pulled to failure but which had the greatest abnormal peak, and an intermediate test to an intermediate level of strain. The multiple tests allowed for the complete mechanical response to be ascertained from approximately 2% true strain until failure, but this resulted in the strain rate varying between approximately 1500 and approximately 3200 s^{-1} across all dynamic tension experiments. There will be a small amount of interpolation error due to strain-rate hardening because of the 2× factor in the rate across experiments; however, it is negligible compared with the noise in the data for each experiment and between specimens. The yield point could only be estimated by manual extrapolation because some amount of the abnormal peak was present even at the lowest total strain. The Appendix shows the individual experiments along with the interpolated true stress–strain curve for the six different dynamic-tension conditions reported herein.

From Figure 4, the general trend in the mechanical response from lowest SFE (TRIP) to highest SFE (Slip) is that TRIP has the lowest yield strength but highest work hardening. Conversely, the Slip alloy has the highest yield strength but lowest work hardening. TWIP is between these two extremes. This trend is true for all conditions tested. Under dynamic compression, the work hardening does drop to approximately zero at higher strains for all three alloys. For dynamic tension, the work hardening stays larger than zero at large strains, especially for the TWIP alloy where the work hardening is essentially constant (~2000 MPa/ε) over the entire plastic regime. TRIP shows a large difference in the strain hardening, especially between the two temperatures tested here (5000–8000 MPa/ε at room temperature and <2000 MPa/ε at 200 °C), which is much more pronounced than the other two alloys. Work hardening for these alloys under the different tested conditions is shown in Figure 8 and will be discussed in more detail in the next paragraph. For the Slip and TWIP alloy, the strain-rate sensitivity at yield is approximately the same in magnitude (~200 MPa increase) between the two alloys and between room temperature and 200 °C. The TRIP alloy is the outlier, where the rate sensitivity at yield is essentially zero under all conditions tested. Additionally, the yield strength increases for the TRIP as temperature increases (by as much as 160%), which is atypical for metals generally. The tension/compression asymmetry in the yield strength is small for all the alloys—less than 10%—at room temperature and drops to essentially zero at the 200 °C testing temperature.

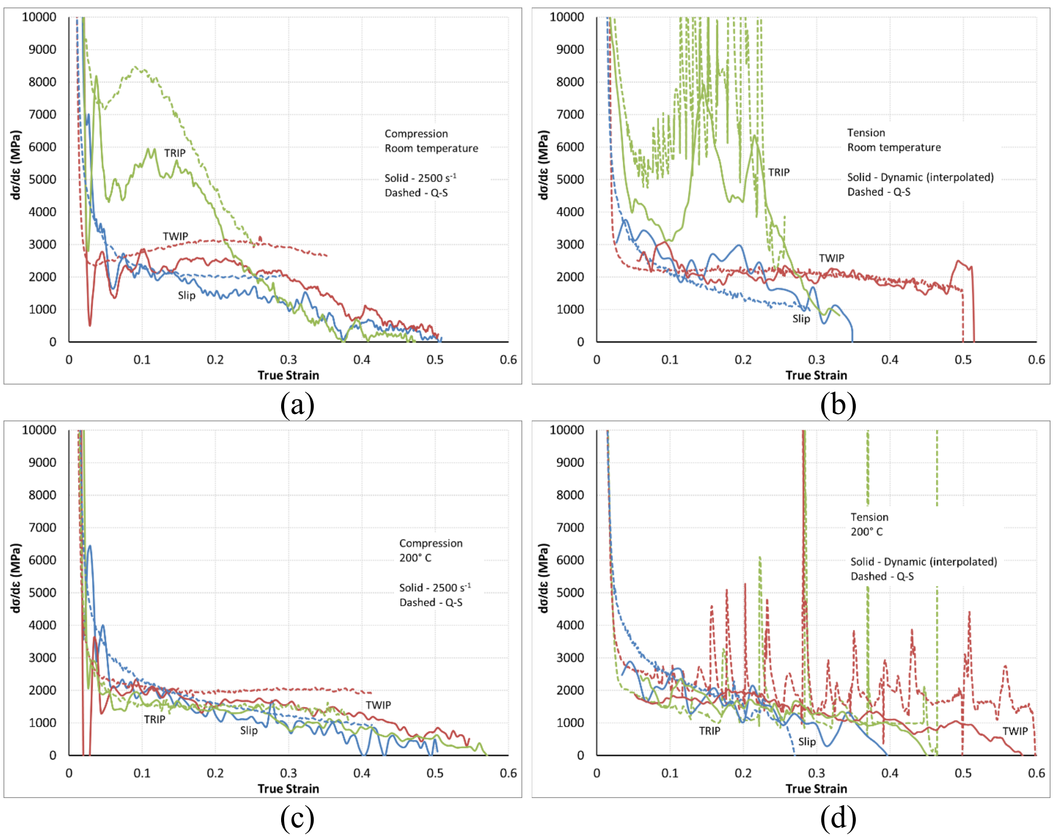

Figure 8. Calculated work-hardening rates of the Slip, TWIP, and TRIP alloys under quasi-static and dynamic deformation at (a) room temperature compression and (b) tension and at (c) 200 °C compression and (d) tension.

The "x" marks in the quasi-static tension data (Figures 4b, 5b, 6b, and 7b) correspond to the ultimate tensile strengths (UTS) for the different alloys. For both the TWIP and TRIP alloys, the UTS occurs at the strain where sample failure occurs (valid conversion to true stress–strain). The UTS for the slip alloy occurs approximately 2%–5% strain prior to sample failure so the true stress–strain values above the UTS are unreliable. The strain-to-failure of the Slip alloy does increase by approximately 5% to 15% from quasi-static to dynamic loading, whereas the

TWIP alloy strain-to-failure is unchanged. The TRIP alloy appears to increase but the extent is unknown because the samples did not fail in dynamic tension. Finally, as expected, the strain-to-failure generally increases as testing temperature increases.

The calculated work hardening in the plastic regime for the three alloys as functions of load path (tension or compression), strain rate, and temperature is summarized in Figure 8. At room temperature, the TRIP alloy has the highest work hardening, followed by the TWIP, and Slip has the lowest. In dynamic compression at room temperature, all the alloys approach a hardening rate of zero above 35% to 40% true strain, whereas in tension the quasi-static and dynamic hardening rates mirror each other over the entire plastic regime. The TRIP alloy is unique where the magnitude of the hardening rate is much higher than the others, the hardening rate drops after yielding (not unique) but rises at intermediate strains before falling precipitously at higher rates. This occurs at both quasi-static and dynamic rates and in tension and compression, even if the hardening magnitudes of the TWIP alloy vary somewhat across the different conditions. The serrated work hardening (and flow; Figure 7b) of the TRIP alloy in quasi-static, room temperature tension is indicative of dynamic strain aging (DSA), which is common in a variety of steels. The serrated flow is caused by dislocation pinning that results in a stress increase, followed by rapid dislocation depinning or multiplication resulting in a stress drop. Mn interacting with stacking faults has been linked to this phenomenon for medium-Mn steels specifically.[27,28] The pinning is caused by C and nitrogen in the interstitials. The TWIP alloy has relatively constant hardening rates, between 2000–3000 MPa/ε under room temperature compression, with quasi-static being a little higher, and approximately 2000 MPa/ε under room temperature tension, and generally independent of rate and plastic strain. At strains above approximately 25%, the TWIP hardening rate exceeds the TRIP, which is the reason why the TWIP has the largest ductility of the three alloys at both quasi-static and dynamic rates. Finally, the Slip alloy at room temperature has the lowest hardening rate, which tends to linearly decrease with plastic strain without any significant strain rate or load path differences.

At a testing temperature of 200 °C, the hardening rates of all three alloys converge in both magnitude and slope under the different conditions tested. The Slip and TWIP alloys only see small drops in hardening rates, but the TRIP rates drop dramatically to be approximately the same as the other two alloys as a function of true strain. Only the TWIP alloy at the quasi-static static strain rate maintains an approximately constant hardening rate (~2000 MPa/ε), whereas the other alloys linearly decrease to a hardening rate of zero at large strains. The serrated flow of the TRIP alloy under quasi-static tensile loading is suppressed but not eliminated at 200 °C. Additionally, the TWIP alloy also shows serrated flow associated with DSA at 200 °C, which was not present at room temperature, quasi-static tensile loading. Thus, increasing the temperature homogenizes the hardening behavior of the three alloys.

These trends observed for the three alloys studied here as functions of strain rate, temperature, and load path are controlled by the SFEs of each alloy and how the experimental parameters modulate the SFE up or down. The TRIP alloy has the lowest SFE, which results in the least stable austenite such that when loaded at room temperature, the γ→ε→α phase transformation begins at the lowest stress value, which causes macroscopic yielding of the material. However, the phase transformation results in significantly higher work-hardening rates for two reasons: 1) the new ε and α grains subdivide the grains of each phase, resulting in a Hall–Petch strengthening effect; and 2) α-martensite is higher strength than the FFC γ-austenite so the material becomes stronger as the α phase fraction increases. However, this hardening rate is strongly influenced by the SFE via the temperature. Increasing the temperature directly increases the SFE, which results in significantly lower hardening rates in both tension and compression as the deformation mechanism shifts to twinning. The phase transformation is fully suppressed at this temperature,[28] which is supported by the rate insensitivity of the behavior at 200 °C—the adiabatic heating does not change the behavior because the static temperature rise has already completely suppressed phase transformation. At room temperature testing, the adiabatic heating caused by dynamic loading reduces the hardening, but moderately, because the temperature rise associated with the approximately 10^3 s^{-1} strain rate tested in this work is less than the 200 °C testing temperature.[29] Thus, phase transformation is only moderately suppressed at this dynamic rate at room temperature, but enough to strongly influence the work hardening.

The TWIP alloy has a higher SFE, so the austenite is more stable under load. This suppresses phase transformation and increases the yield strength relative to the TRIP alloy, but since the alloy is fully austenitic, it yields via dislocation glide at a lower strength relative to the Slip alloy. The intermediate SFE promotes twinning, but a critical dislocation density is required before twinning dominates, which occurs when the work-hardening rate reaches an approximately constant value[27] at a few percent strain at room temperature. The subsequent hardening rate is lower than TRIP because the only hardening mechanism is twinning, which subdivides the grains and results in a Hall–Petch strengthening effect. Increasing the temperature raises the SFE and increases critical dislocation density, which delays twinning dominating the deformation to higher strains and creates a more gradual transition in the work-hardening curve—or suppresses the twinning completely if the temperature is high enough. Increasing the strain rate tends to promote twinning; however, this is counteracted by the rise in temperature due to plastic work and adiabatic heating at dynamic rates, which increases the SFE shifting the deformation mechanism toward dislocation slip. The SFE also decreases as the total strain increases, which moderates that shift in mechanisms. Finally, at 200 °C in tension, the occurrence of DSA slows the increase in the SFE, promoting twinning, which maintains a higher hardening rate (~2000 MPa/ε; Figure 8d) than would be expected. The TWIP alloy is a complex interaction of factors that either raise or lower the SFE but because they partially balance each other, the result is a material that maintains moderate strength combined with high work hardening and ductility over a relatively wide range of strain rates, total strains, and temperatures versus typical martensitic steels.

Finally, the Slip alloy has the highest SFE, which suppresses both phase transformation and twinning such that only dislocation glide accommodates the deformation. This means the yield strength is the highest since it is approximately 25% δ-ferrite, but the work hardening is the lowest because dislocation generation has a smaller hardening effect than the other mechanisms. Specifically, Magagnosc et al.[30] showed the mechanical behavior is due to the duplex microstructure of the Slip alloy. The stronger, fine-grained δ-ferrite delays macroscopic yielding even after the weaker, coarse-grained γ-austenite begins to yield. After macro-yielding, the now deforming δ-ferrite maintains high strength, while the still deforming γ-austenite imparts good work hardening and ductility compared with typical fully martensitic steels. The SFE increases at elevated temperatures, which preserves the dislocation motion-based deformation mechanism but the δ-ferrite thermally softens, which reduces the strength overall with only a relatively small drop in the work-hardening rate.

4. Conclusions

Three AHSS alloys with a common Fe–Mn–Al–Cr–C base composition were fabricated with varying SFEs to isolate dislocation glide, twinning, and phase transformation as the dominant deformation mechanism. The changes in the mechanical behavior were measured as functions of strain rate, temperature, and load path (tension or compression) which is linked to the changes in the SFE under the various conditions. The overall conclusions are presented in the following paragraphs.

The Slip alloy has the highest yield strength but lowest work-hardening rate, while the TRIP alloy has the lowest yield strength and highest work-hardening rate, with the TWIP alloy between the two at room temperature at both quasi-static and dynamic strain rates and in tension and compression. The γ→ε→α phase transformation of the TRIP alloy maximizes hardening by new ε and α grains subdividing the grains, resulting in a Hall–Petch strengthening effect, and α is higher strength than γ so the material becomes stronger as the α phase fraction increases. The moderate hardening of the TWIP alloy is created by the single mechanism of twins subdividing the grains and leading to a Hall–Petch strengthening effect. The dislocation glide of the Slip alloy is least effective at work hardening the material.

Increasing the temperature homogenizes the behavior of the three alloys. The Slip and TWIP alloys' yield strengths drop and the work-hardening rate drops only a small amount. However, the TRIP alloy's yield strength increases with a dramatic drop in the work hardening. The rise of the SFE with temperature causes the TRIP alloy behavior to shift toward that of the TWIP, and the TWIP becomes more like the Slip alloy. However, the shift in the TWIP behavior is moderated by the occurrence of DSA under quasi-static tensile loading which reduces the rise in the SFE, which reduces the drop in the work hardening.

For the Slip and TWIP alloys, the strain-rate sensitivity increases the yield strength but little change in the work-hardening rate is observed. The TRIP alloy is the opposite, where the change in the yield strength is minimal, but the subsequent work hardening is reduced substantially. At dynamic strain rates, the adiabatic heating that occurs increases the SFE which only increases as the strain increases. Thus, the TRIP behavior shifts toward the TWIP behavior and the TWIP toward the Slip alloy behavior, in the same manner as increasing the testing temperature did, but these shifts are moderated somewhat by the increase in strain (reduces the rise of the SFE) and twinning activity increases as the strain rate increases.

5. References

1. Dumay A, Chateau J, Allain S, Migot S, Bouaziz O. Influence of addition elements on the stacking-fault energy and mechanical properties of an austenitic Fe-Mn-C steel. Mat Sci Eng A. 2008;483–484:184–187.

2. De Cooman B, Estrin Y, Kim S. Twinning-induced plasticity (TWIP) steels. Acta Mat. 2018;142:283–362.

3. Pierce D, Jimenez J, Bentley J, Raabe D, Wittig J. The influence of stacking fault energy on the microstructural and strain-hardening evolution of Fe-Mn-Al-Si steels during tensile deformation. Acta Mat. 2015;100:178–190.

4. Field D, Qing J, Aken DV. Chemistry and properties of medium-Mn two-stage TRIP steels. Metall Mat Trans A. 2018;49(10):4615–4632.

5. Field D, Aken DV. Dynamic strain aging phenomena and tensile response of medium-Mn TRIP steel. Metall Mat Trans A. 2018;49(4):1152–1166.

6. Lloyd J, Field D, Limmer K. A four parameter hardening model for TWIP and TRIP steels. Mater Des. 2020;194108878.

7. Field D, Garza-Martinez L, Aken DV. Processing and properties of medium-Mn TRIP steel to obtain a two-stage TRIP behavior. Metall Mat Trans A. 2020;51:4427–4433.

8. Pozuelo M, Wittig J, Jimenez J, Frommeyer G. Enhanced mechanical properties of a novel high-nitrogen Cr-Mn-Ni-Si austenitic stainless steel via TWIP/TRIP effects. Metall Mat Trans A. 2009;40(8):1826–1834.

9. Allain S, Chateau J, Bouaziz O. A physical model of the twinning-induced plasticity effect in a high manganese austenitic steel. Mat Sci Eng A. 2004;387–389:143–147.

10. Allain S, Chateau J, Bouaziz O, Migot S, Guelton N. Correlations between the calculated stacking fault energy and the plasticity mechanisms in Fe-Mn-C alloys. Mat Sci Eng A. 2004;387–389:158–162.

11. Saeed-Akbari A, Imlau J, Prahl U, Bleck W. Derivation and variation in composition-dependent stacking fault energy maps based on subregular solution model in high-manganese steels. metall. Mat Trans A. 2009;40(13):3076–3090.

12. Benzing J et al. Effects of strain rate on mechanical properties and deformation behavior of an austenitic Fe-25Mn-3Al-3Si TWIP-TRIP steel. Mat Sci Eng A. 2018;711:78–92.

13. Curtze S, Kuokkala V. Dependence of tensile deformation behavior of TWIP steels on stacking fault energy, temperature and strain rate. Acta Mat. 2010;58(15):5129–5141.

14. Frommeyer G, Brux U, Neumann P. Supra-ductile and high-strength manganese-TRIP/TWIP steels for high energy absorption purposes. ISJ Inter. 2003;43:438–446.

15. Grassel O, Kruger L, Frommeyer G, Meyer L. High strength Fe-Mn-(Al, Si) TRIP/TWIP steel development—properties—application. Int J Plasticity. 2000;16(10–11):1391–1409.

16. Chung K et al. Formability of TWIP (twinning induced plasticity) automotive steels. Int J Plasticity. 2011;27:52–81.

17. Zhang J et al. Microstructures, mechanical properties and deformation of near-rapidly solidified low-density Fe-20Mn-9Al-1.2C-xCr steels. Mater Des. 2020;186:108307.

18. Field D, Limmer K. Effect of solution treatment on grain size and toughness of lightweight Fe-Mn-Al-C steel. Proceedings of the Iron & Steel Technology Conference (AISTech 2019); 2019 May 6–9; Pittsburgh, PA. AIST; 2019.

19. Field D, Limmer K, Hornbuckle B. On the grain growth kinetics of a low density steel. Metals. 2019;9(9):997.

20. Kecskes L et al. Evaluation of a belt-cast austenitic steel alloy from Salzgitter Mannesmann Forschung: effect of hardness on the ballistic resistane against two 0.30-cal. projectile types. Army Research Laboratory (US); 2017 Aug. Report No.: ARL-TR-8080.

21. Olson G, Cohen M. A general mechanism of martensitic nucleation: part I. General concepts and the FCC to HCP transformation. Metall Trans A. 1976;7(12):1897–1904.

22. Pisarik S, Aken DV. Thermodynamic driving force of the gamma to epsilon transformation and resulting MS temperature in high-Mn steels. Metall Mat Trans A. 2015;47(3):1009–1018.

23. Chen W, Song B. Split Hopkinson (Kolsky) bar: design, testing and applications. Springer, 2011.

24. Nemat-Nasser S. High strain rate testing. In: Kuhn H, Medlin D, editors. ASM handbook: mechanical testing and evaluation. 8th vol. ASM International; 2000. p. 427–428.

25. Limmer K et al. Designing steels to mitigate failure during ballistic deformation (summary technical report, Oct 2018–Sept 2021). DEVCOM Army Research Laboratory (US); 2022 Mar. Report No.: ARL-TR-9424.

26. Song B, Antoun B. Pseudo stress response in Kolsky tension bar experiments. Exp Mech. 2012;52:525–528.

27. Magagnosc D et al. Temperature and stress dependent twinning behavior in a fully austenitic medium-Mn steel. Acta Mat. 2022;231:117864.

28. Field D, Magagnosc D, Hornbuckle B, Lloyd J, Limmer K. Manipulation of the stacking fault energy of a medium-Mn steel through temperature and hierarchical compositional variation. Metall Mat Trans A. 2024;55A:161–172.

29. Lloyd J, Magagnosc D, Meredith C, Limmer K, Field D. Improved dynamic strength of TRIP steel via pre-straining. Scripta Mat. 2022;220:114941.

30. Magagnosc D et al. Superior strength and ductility in a low density duplex steel studied by in situ neutron diffraction. Mat. Sci Eng A. 2021;799:140252.

Appendix. Dynamic Tension Interpolation

The separate dynamic tension experiments for each alloy at room temperature and 200 °C are shown in the figures below as dashed lines. Each experiment goes to a different strain-to-failure and results in a different amount of the pseudo-stress response at and after yield. Thus, a single response curve for each condition was manually interpolated from the multiple experiments at each condition. This results in smoothed-out responses that can be compared with quasi-static and dynamic compression and tension responses so trends can be identified and certain properties calculated or approximated.

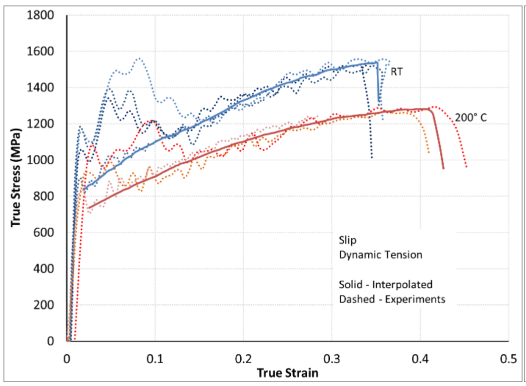

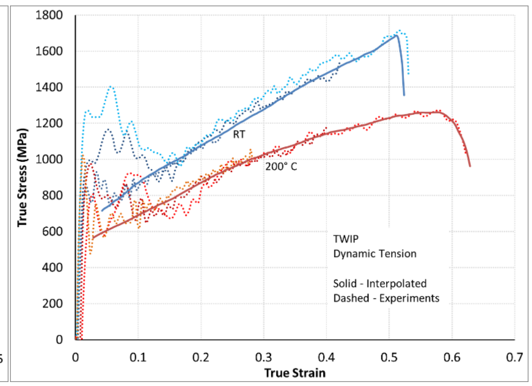

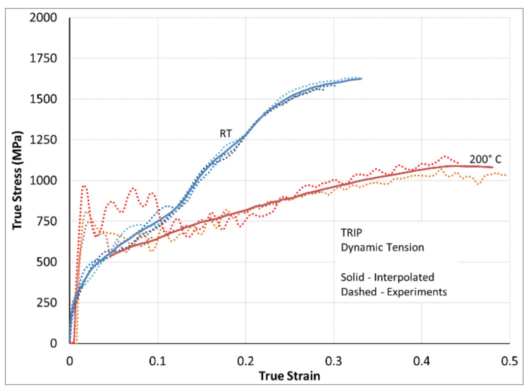

List of Symbols, Abbreviations, and Acronyms

3D	Three-Dimensional
AHSS	Advanced High-Strength Steels
Al	Aluminum
C	Carbon
Cr	Chromium
DIC	Digital Image Correlation
DSA	Dynamic Strain Aging
EBSD	Electron Backscatter Diffraction
Fe	Iron
IR	Infrared
Mn	Manganese
SFE	Stacking-Fault Energy
Si	Silicon
TRIP	Transformation-Induced Plasticity
TWIP	Twinning-Induced Plasticity
UTS	Ultimate Tensile Strengths

1 (PDF)	DEFENSE TECHNICAL INFORMATION CTR DTIC OCA
1 (PDF)	DEVCOM ARL FCDD RLB CB TECH LIB